ACS EARTH AND SPACE CHEMISTRY

http://pubs.acs.org/journal/aesccq

Article

Water Adsorption on Hydroxyapatite and Struvite as a Function of Relative Humidity: Application of BET and Freundlich Adsorption Models

Manoj Silva, John P. Baltrus, Daniel J. Burnett, and Jonas Baltrusaitis*

Cite This: *ACS Earth Space Chem.* 2022, 6, 431−443

Read Online

ACCESS | Metrics & More | Article Recommendations

ABSTRACT: Anthropogenically derived phosphate-bearing crystalline materials serve as reactive surfaces for nutrient recycling to the environment. The reactivity of these surfaces is critical for controlling nutrient release rates and will depend on the relative humidity at the soil surface. In this study, we investigate water uptake on these phosphate-bearing minerals as a function of relative humidity. In particular, this study is focused on the water adsorption properties of two anthropogenically derived phosphates, hydroxyapatite (HAP) and struvite. HAP exhibited a stable surface structure, and the water adsorption data were fit using Brunauer−Emmett−Teller (BET) and Freundlich adsorption models. Struvite surface, on the other hand, exhibited intrinsic instability due to the crystalline water loss at very low relative humidity, leading to the adsorption data not being well described by traditional models. Diffuse reflectance infrared spectroscopy studies showed that a relative humidity of <5% resulted in crystalline water removal, as well as the change in the structure of the hydrogen-bonded surface water and the ammonium ions in the struvite crystals. HAP exhibited a calculated heat of sorption that converged to the water heat of liquefication, while struvite exhibited transient behavior, which resulted in a nonconvergent calculated heat of sorption.

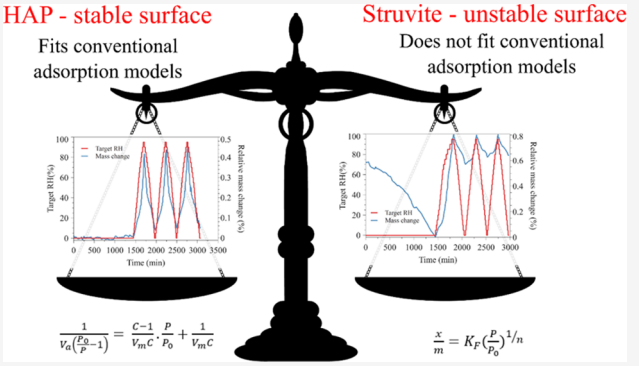

KEYWORDS: *struvite, hydroxyapatite, relative humidity, adsorption, Freundlich, BET*

Downloaded via LEHIGH UNIV on August 31, 2022 at 17:29:25 (UTC).
See https://pubs.acs.org/sharingguidelines for options on how to legitimately share published articles.

INTRODUCTION

The understanding of environmental water vapor uptake as a function of relative humidity (RH) on the crystalline materials of anthropogenic origin containing nitrogen (N) and phosphorus (P) in the form of NH_4^+ and/or PO_4^{3-} ions remains very low compared to that on the natural minerals, which are chiefly comprised of oxides/hydroxides or carbonates.[1−4] Recent studies investigated water uptake as relative humidity on certain complex anthropogenically derived combustion products, such as fly ash,[5−7] that can become incorporated into mineral dust and affect the atmospheric environment, climate, and hydrological cycles. Emission flux and atmospheric loading of these combustion process-generated particles, chiefly coal fly ash, account for ∼300 million U.S. tons annually, while natural minerals have been estimated to reach some 2 billion U.S. tons annually.[5,8,9] Importantly, both natural and anthropogenic particles have been shown to undergo environmental processing, such as atmospheric transport and aging, and contribute significant sources of nutrients to the environment.[10] For example, mineral dust was shown to be an important external source of phosphorus to the ocean[11] or Amazon rainforest.[12] Similarly, anthropogenic phosphates derived due to the soil erosion of cleared land and biomass burning can also contribute a significant fraction of phosphorus to the ocean.[13] Finally, enhanced phosphorus influx into the environment in the form of aqueous PO_4^{3-} ion via surface waterways due to the disrupted nutrient cycles has led to major water quality concerns including eutrophication and harmful algal blooms, which can have lasting environmental and economic impacts.[14−19]

The above-mentioned natural and anthropogenic sources of phosphorus to the environment, while contributing a large total phosphorus amount, contain rather low nutrient concentrations. For example, volcanic emission sources of phosphorus, recognized to have high phosphorus flux into localized areas over short time scales, contain only up to 1%.[10,20] Similarly, Saharan dust contains on average 0.09% of

Received: November 17, 2021
Revised: January 19, 2022
Accepted: January 25, 2022
Published: February 3, 2022

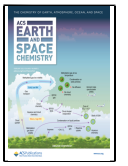

ACS Publications

© 2022 American Chemical Society

phosphorus[10,21] and chiefly contributes to this nutrient due to the large overall flux. A new and emerging source of the reactive highly concentrated phosphorus and nitrogen can be considered anthropogenically derived fertilizer materials obtained during the wastewater treatment process via reaction of the NH_4^+ and PO_4^{3-} ion-containing water with magnesium and calcium-containing minerals.[22−27] Struvite, $MgNH_4PO_4 \cdot 6H_2O$, and hydroxyapatite (HAP), $Ca_{10}(PO_4)_6(OH)_2$, are obtained in increasing amounts and returned into the environment as green fertilizers.[28−31] Differently from natural and other anthropogenic nitrogen- and phosphorus-containing sources (excluding mineral fertilizers), they contain significant concentrations of nutrients, e.g., 13% of P and 6% of N and 18% P, respectively. These crystalline materials of anthropogenic origin span a rather large solubility range with solubility product constant, K_{sp}, ranging from 2×10^{-13} to 2.9×10^{-58} for struvite and HAP, respectively, and due to their low solubility are expected to remain with the environment for extended periods.[32,33] Importantly, the hygroscopicity of these materials will affect their particle size, reactivity, and, ultimately, NH_4^+ and PO_4^{3-} ion releases into the environment. The literature on water vapor adsorption as a function of relative humidity on HAP and struvite is limited, with some recent work focusing on understanding the effects of Ca/P ratio on water adsorption on HAP, as well as the effect of particle size on the number of adsorbed water layers on nano-HAP.[34,35] Correspondingly, the hygroscopic properties of struvite and HAP are not well understood even though they may lead to significant negative environmental effects via water vapor facilitated nutrient release, such as watershed eutrophication or reactive N-gas (such as N_2O or NH_3) release.

In this work, dynamic vapor sorption (DVS) experiments were utilized to investigate water uptake on struvite and hydroxyapatite particles. DVS has emerged as a useful technique in understanding the interactions between various mineral interfaces and water under varying relative humidity (RH) conditions, as it provides adsorption data that can be used to investigate isotherms using various sorption model fits.[36,37] In particular, DVS was employed to measure the mass of water adsorbed as a function of relative humidity at a temperature of 25 °C (as measured using the onboard temperature probe). All samples were systematically characterized by powder X-ray diffraction (pXRD), Raman spectroscopy, scanning electron microscopy (SEM), diffuse reflectance infrared spectroscopy (DRIFTS), and X-ray photoelectron spectroscopy (XPS) before water uptake experiments.

MATERIALS AND METHODS

Materials. The struvite was obtained from Alfa Aesar (98%), and hydroxyapatite was obtained from Millipore-Sigma (99%). Both materials were used as received.

Dynamic Vapor Sorption (DVS) Experiments. The DVS intrinsic (surface measurement systems) was used for all DVS experiments. Figure 1 shows the schematic representation of the experimental setup. Sample powder (20 mg) was loaded into the sample pan and exposed to dry airflow for a set time to remove weakly bound water from the surface. This period was different between the struvite and HAP. HAP was dried for 24 h, while struvite was dried for 10 min (discussed *vide infra*). After the drying period, the relative humidity was increased from 0 to 95% and then decreased back to 0% in increments of 5%. During each cycle, the adsorbed mass was recorded as a function of time until the mass change rate (dm/dt) was under

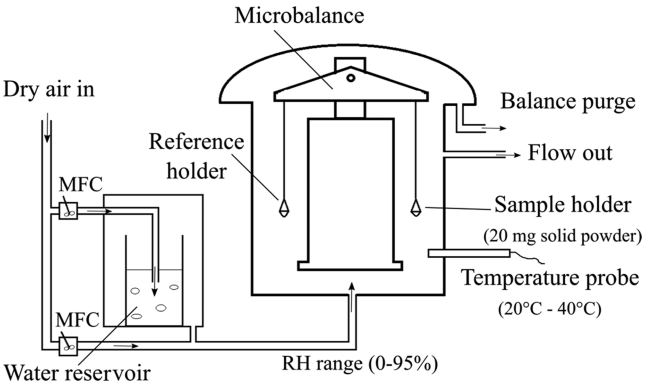

Figure 1. Schematic representation of the dynamic vapor sorption experimental setup.

0.002 mg/min where equilibrium was assumed. A probe in the sample chamber was used to constantly measure temperature and keep a constant 25 °C temperature. The SMS DVS Analysis Suite software package was used to perform data analysis functions such as baseline correction, isotherm calculation, and heat of sorption analysis.

Powder X-ray Diffraction. The pXRD patterns were acquired using an Empyrean, PANalytical B.V. diffractometer. The applied current was 40 mA, and the applied voltage was 45 kV. The X-ray mirror that was used was a graded, flat Bragg−Brentano HD mirror, and the step size that was used for the measurements was 0.0131°. The diffraction patterns were obtained between 5 and 70°. The radiation source used was Cu Kα1,2 with Cu Kα1 wavelength 1.540598 Å and Cu Kα2 wavelength 1.544426 Å. The ratio of Kα1/Kα2 was 0.5. The analysis was performed with a 4 mm mask, 1/8″ incident beam divergence slit, 1/2″ incident beam antiscatter slit, 7.5 mm diffracted beam antiscatter slit, and a 0.04 mm Soller slit. The powder was placed on a glass slide and pressed into a 1 cm × 1 cm sized smooth powder film.

Raman Spectroscopy. Raman spectra were acquired using a WITec alpha300R confocal Raman microscope using 532 nm laser, a Zeiss EC Epiplan-Neofluar 100×/0.9 objective, G2: 600 g/mm grating, and a 3 s integration time per point. The spectral range was 100−4000 cm^{-1} with the center at 2000 cm^{-1}, and the spectral resolution was ∼2 cm^{-1}. Before each experiment, the instrument was calibrated using a Si wafer. Laser intensity at the sample was ∼54 mW.

Scanning Electron Microscopy. All SEM images were obtained using a Hitachi 4300 SE FE-SEM. A 5.0 kV voltage setting was used.

X-ray Photoelectron Spectroscopy (XPS). XPS analysis was carried out with a ULVAC-PHI VersaProbe III instrument using a monochromatized Al Kα X-ray source (1486.6 eV). The pass energy of the analyzer was 55.5 eV, the acquisition area had a diameter of 100 μm, and the scan step size was 0.1 eV. Binding energies were corrected for charging by referencing the C 1s peak at 285.0 eV. CasaXPS was used for spectral processing and quantification.[38]

Diffuse Reflectance Infrared Fourier Transformed Spectroscopy (DRIFTS). A Thermo Nicolet iS50 infrared spectrometer equipped with a mercury−cadmium−tellurium (MCT) liquid nitrogen-cooled detector was used in combination with a Harrick Praying Mantis diffuse reflection accessory equipped with KBr windows. About 30 mg of the powder was loaded into the DRIFTS cell. The spectra were acquired under

https://doi.org/10.1021/acsearthspacechem.1c00406
ACS Earth Space Chem. 2022, 6, 431−443

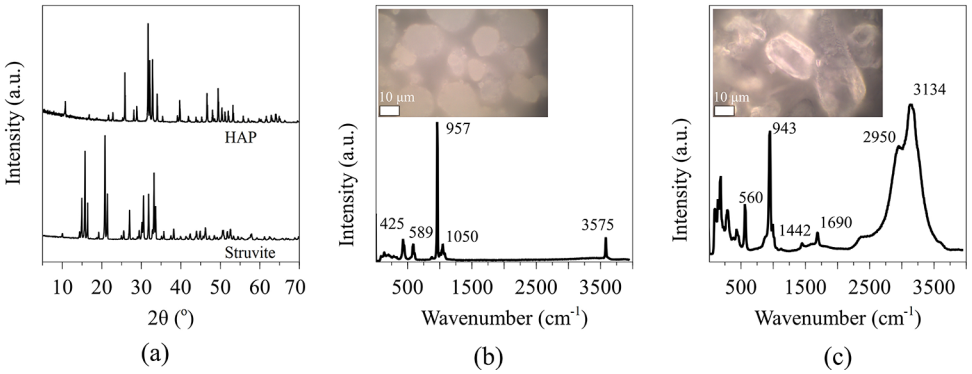

Figure 2. (a) pXRD patterns of struvite and HAP. (b) Struvite and (c) HAP Raman spectra.

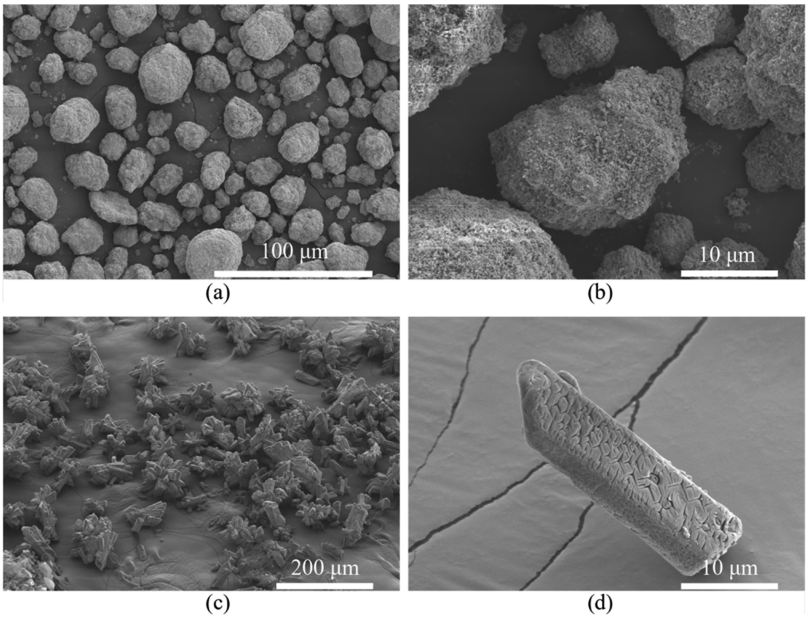

Figure 3. SEM of (a,b) HAP and (c,d) struvite.

a 30 mL/min dry airflow (the same dry air as used in the DVS instrument). All spectra were averaged over 96 scans at a resolution of 4 cm^{-1}. The CO_2 adsorption experiment on struvite was conducted by drying the struvite under N_2 for 24 h, exposing it to a mixture of CO_2/N_2 for 30 min and subsequently flowing N_2 for 30 min to remove the weakly physisorbed species. Spectra were taken at the initial state with a mirror reference after 24 h of drying and after CO_2 adsorption and N_2 exposure.

RESULTS AND DISCUSSION

Physicochemical Characterization of Hydroxyapatite and Struvite Crystals. XRD was used to characterize the crystalline composition of HAP and struvite (shown in Figure 2a). HAP is typically present in the hexagonal crystal structure (space group $P6_3/m$), and the HAP sample analyzed in this study showed good agreement with the reference pattern.[39] The HAP lattice parameters are reported as $a = b = 9.432$ Å and $c = 6.881$ Å.[40] HAP in its stoichiometric formula $Ca_{10}(PO_4)_6(OH)_2$ exhibits a Ca/P molar ratio of 1.67, although HAP may be present as a mixture of calcium phosphate phases, which leads to nonstoichiometric Ca/P ratios.[41] The most thermodynamically stable form of HAP crystallizes in the monoclinic structure but is only found at high temperatures. The hexagonal HAP structure, which is dominant at ambient conditions due to its stability, may contain a minor fraction of nonstoichiometric Ca/P.

Struvite possesses the orthorhombic crystal structure and belongs to the space group $Pmn2_1$ with the lattice parameters $a = 6.9650$ Å, $b = 6.1165$ Å, and $c = 11.2056$ Å.[2,42] Magnesium phosphate hydrates typically form in the orthorhombic crystal structure, with $Mg_3(PO_4)_2{\cdot}4H_2O$ belonging to $Cmc21$ and $Mg_3(PO_4)_2{\cdot}8H_2O$ to $C2/c$ space groups.[43,44] Furthermore, struvite can form isomorphous analogues by replacing the NH_4^+ with K^+ and Na^+ and replacing the PO_4^{3-} with AsO_4^{3-}.[45−47] The struvite XRD pattern showed an agreement with previous literature reports.[22]

The Raman spectra for HAP and struvite are shown in Figure 2b,c, respectively, together with the corresponding optical images of the crystals. The symmetric ν_1 phosphate stretch for HAP is located at 957 cm^{-1}, with the asymmetric ν_3 phosphate stretch located at 1050 cm^{-1}.[48] The ν_2 O−P−O bending mode is located around 425 cm^{-1}, and the ν_4 mode corresponds to the peak at 589 cm^{-1}.[48] The symmetric ν_1 phosphate stretch for struvite is located at 943 cm^{-1}, while the ν_4 mode corresponds to 560 cm^{-1}.[48,49] The hydrogen-bonded hydroxyl/water and ammonium species lead to the increase of a prominent region in struvite, with a broad band centered

https://doi.org/10.1021/acsearthspacechem.1c00406
ACS Earth Space Chem. 2022, 6, 431−443

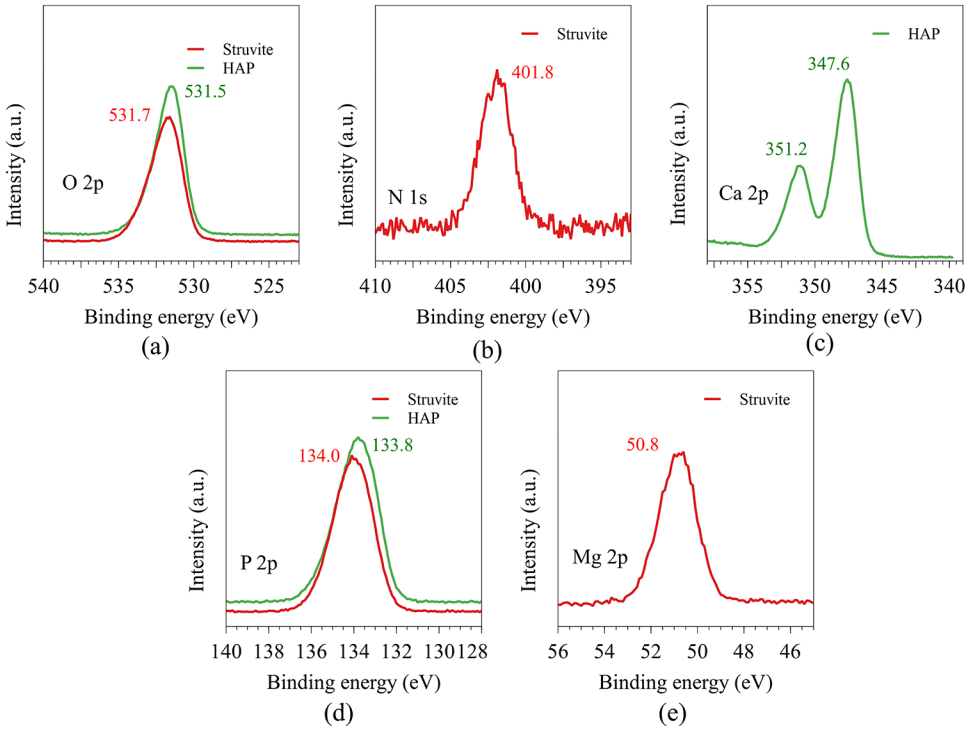

Figure 4. High-resolution X-ray photoelectron spectra of HAP and struvite: (a) O 2p, (b) N 1s, (c) Ca 2p, (d) P 2p, and (e) Mg 2p regions.

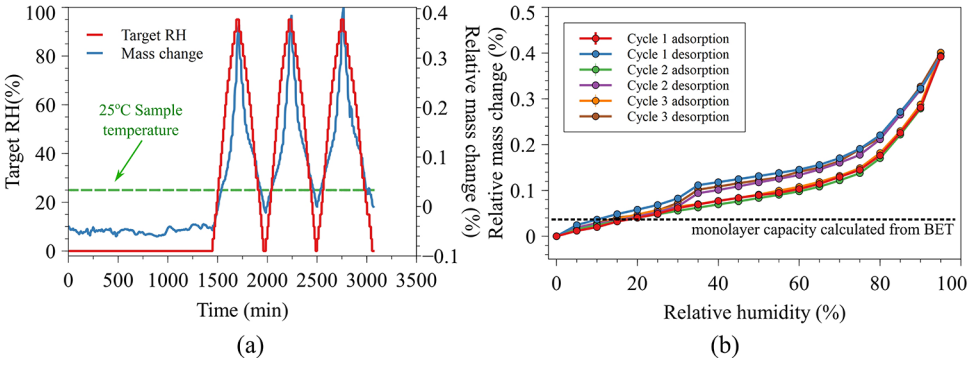

Figure 5. (a) Relative mass change as a function of time for HAP. (b) Water adsorption isotherms on HAP during three consecutive cycles.

around 3134 cm^{-1} and a shoulder around 2950 cm^{-1}.[47,50] The hydroxyl region of HAP does not exhibit similar broad peaks due to the lack of crystal water but the sharp 3575 cm^{-1} peak corresponds to the OH stretching mode.[48] Struvite contains tetrahedral NH_4^+ groups, as evidenced by the 1442 and 1690 cm^{-1} peaks.[47,50]

The particle morphology was studied using SEM. Figure 3a,b shows the images for HAP particles. The HAP particles exhibit complex structures in the macroscopic images comprised of a wide range of particle sizes. The particle shapes are not well defined, and the size range is around 5−50 μm. Struvite SEM images are shown in Figure 3c,d. The pyramidal struvite crystals were observed, in agreement with the primary shape reported in previous work.[22,51,52] The struvite crystals were in the 20−50 μm size range. As shown in Figure 3d, the struvite crystals exhibit Y-shaped cracks on the surface, which are attributed to artifacts formed under a high vacuum during SEM imaging.[53]

XPS was used to study the surface region of the HAP and struvite crystals, as shown in Figure 4. The O 1s peaks are closely aligned between HAP and struvite, as they centered around 531.6 eV in agreement with the literature values.[54] Struvite contains ammonium ions leading to the N 1s XPS peak, which is centered around 401.8 eV, in agreement with previous reports.[55] HAP and struvite contain Ca^{2+} and Mg^{2+}, respectively, with 2p peaks centered around 347.6 and 50.8 eV, respectively.[54,56,57] The P 2p region for HAP is centered around 133.8 eV, while struvite is at 134.0 eV.[54,55,57] The ratio of Ca/P in the HAP sample used in this study was found to be 1.14 *via* the XPS peak ratio of Ca 2p/P 2p, which is P-enriched compared to that of previous literature reports.[34,58] This Ca/P ratio is for the surface region as it is measured using XPS, while the bulk Ca/P may differ.[58]

Water Adsorption Measurements as Relative Humidity. The water adsorption isotherms for the three consecutive cycles of adsorption−desorption, as well as the relative mass change as a function of time for HAP, are shown in Figure 5. The relative mass change is defined as the percentage of mass change compared to the initial mass of the sample (at t = 0). Prior to the water adsorption, HAP and struvite were dried

https://doi.org/10.1021/acsearthspacechem.1c00406
ACS Earth Space Chem. 2022, 6, 431−443

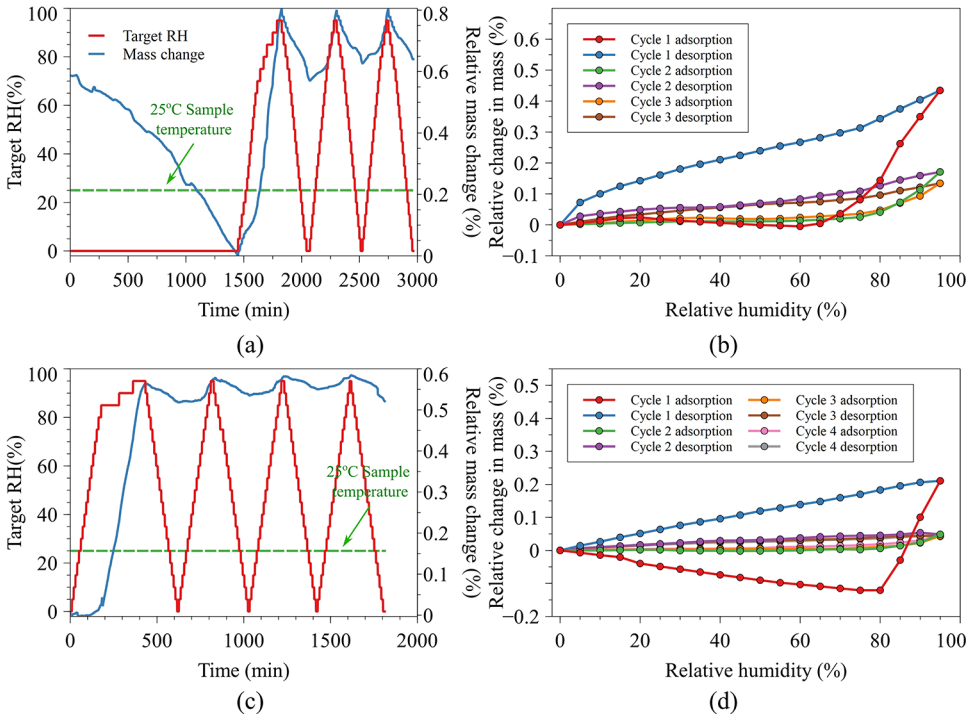

Figure 6. (a) Relative mass change as a function of time for struvite with 24 h of drying. (b) Water adsorption isotherms for struvite with 24 h of drying. (c) Relative mass change as a function of time for struvite with 10 min of drying. (d) Water adsorption isotherms for struvite with 10 min of drying.

under dry air (0% RH) for 24 h to remove any physisorbed water and the sample mass was measured to assess the stability of the sample under the dry airflow. Previous work on struvite has demonstrated that struvite decomposition occurs under 100 °C, and as such, temperature treatment with the goal of removing all preadsorbed water without changing the sample composition would be impossible.[53,59] In the case of HAP, due to the presence of structured water molecule stacking along the vertical axis along with its characteristic OH^- channels, even at 800 °C, surface adsorbed water is present.[60,61] Therefore, temperature pretreatment steps to remove strongly adsorbed surface water cannot be applied to these two materials. As such, the drying step is limited to only removing the weakly bound physisorbed water, as this study intends to investigate the interactions between phosphate-bearing mineral interfaces and water under environmentally relevant conditions.

HAP exhibited very weak hygroscopic behavior, as evidenced by the low mass change as a function of the time plot in Figure 5a. Furthermore, during the drying stage, HAP shows no significant mass change, indicating stability under the drying conditions. The isotherm in Figure 5b showed a maximum relative mass increase of 0.40% at 95% RH. The shape of the isotherm is similar to previously reported water adsorption isotherms for HAP.[62] Both HAP and struvite isotherms exhibit a shape that is similar to that of type II, which is indicative of a nonporous or macroporous material.[63] The unrestricted monolayer−multilayer adsorption gives rise to the type II shape, while the gradual increase of the intermediate linear region (under 35% RH) without a clear knee indicates that the monolayer formation and multilayer adsorption have a significant overlap without clear definition. As demonstrated in previous work, HAP leads to the type II isotherm with a hysteresis loop, which is a slight deviation from type II isotherm behavior, but due to the lack of significant mesoporosity, it does not display type IV isotherm behavior.[34,64] During the drying stage, HAP exhibits no significant variation of mass, indicating that it is stable under the dry airflow and does not undergo any transformation or loss of mass. For all three relative humidity exposure cycles, the HAP water uptake remains very consistent with minimal variation as shown by the isotherms, indicating a stable surface that does not undergo dissolution or restructuring that is common in more hygroscopic materials.[65−67] This is due to the largely insoluble nature of HAP that is evidenced by the low K_{sp} value. A minor but consistent hysteresis loop was observed for the HAP isotherms in agreement with literature data.[34,68,69] Over the second and third stages, the hysteresis loop reaches a constant shape. Previous work on HAP has shown that irreversible water adsorption can occur on HAP due to the ability of water to incorporate into the HAP crystal lattice.[34] A small fraction of the adsorbed water can deprotonate and react with HAP, forming crystal H_2O with OH^- and HPO_4^{2-} with PO_4^{3-}.[70] This hydration of HAP irreversibly occurs when the Ca/P ratio is low (Ca/P = 1.3) and can cause up to 1% distortion of the (002) interplanar distance, whereas a high Ca/P ratio HAP (Ca/P = 1.6) does not irreversibly adsorb water in sufficient quantity to exhibit such lattice distortion that is detectable.[34] The isotherm shape and hysteresis type exhibited by the HAP used in this study agree with the previous work done on Ca/P = 1.3 HAP.[34] It is, however, important to note that most HAP samples are often heterogeneous in composition, with the surface region and the bulk structure containing different Ca/P ratios due to differing methods of preparation.[58,60] And while such Ca/P ratio changes can induce slightly different water adsorption behavior, the stability of the HAP bulk crystal structure is not significantly altered, as the XRD pattern is reported to remain largely unchanged.[34] Therefore, it can be concluded

https://doi.org/10.1021/acsearthspacechem.1c00406
ACS Earth Space Chem. 2022, 6, 431−443

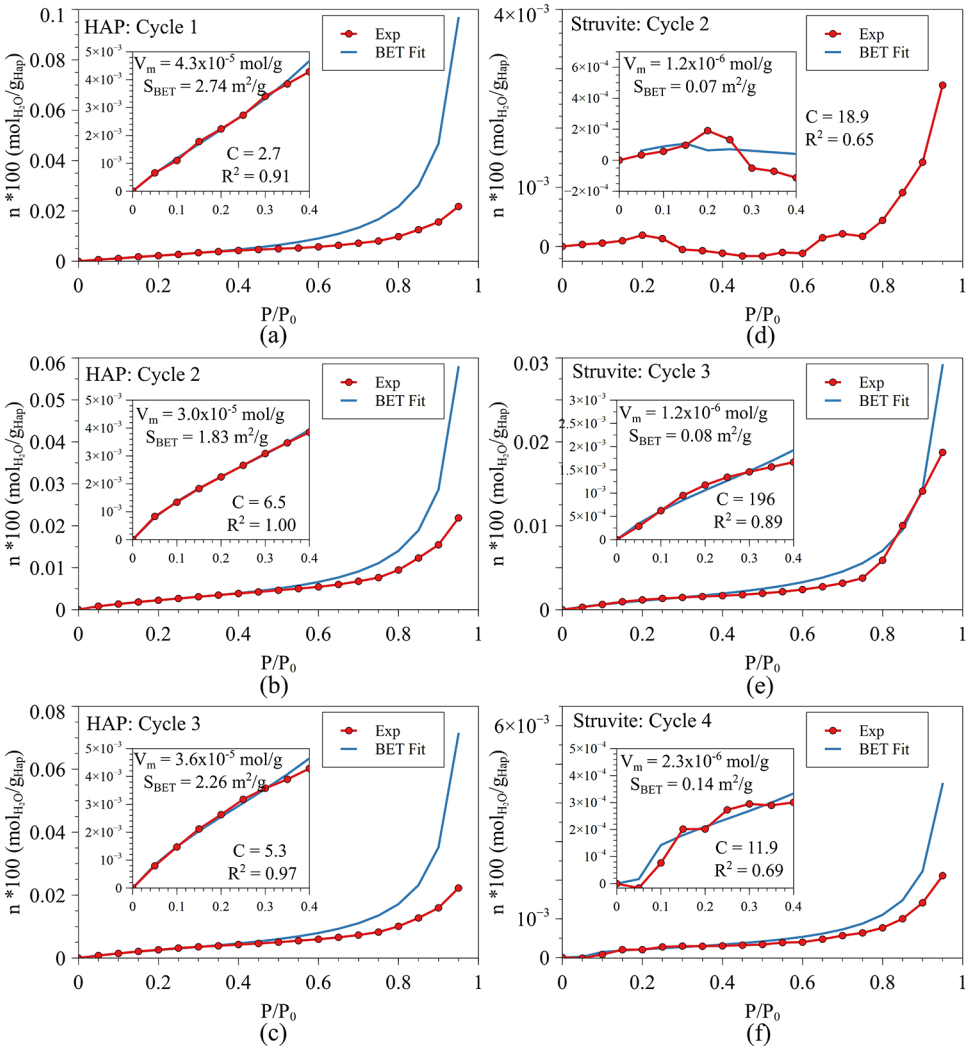

Figure 7. BET adsorption isotherms for (a)−(c) HAP and (d)−(f) struvite.

that irreversible water adsorption occurs over the first cycle of the RH ramp, and HAP remains highly stable over subsequent cycles.

In contrast to HAP, which showed effectively no relative mass change during the drying period, struvite showed a significant mass loss during the drying stage. Figure 6a shows the mass loss for struvite starting at 0.58% and continuing over the 24 h drying period preceding the relative humidity adsorption−desorption cycles. As shown in Figure 6b, isotherms were acquired, and struvite exhibits a significant variation in the relative mass change between the first cycle and the two subsequent cycles. The initial mass loss shown in Figure 6a is attributed to a combination of the loss of water molecules weakly bound to the surface as well as some of the water contained in the bulk crystal structure (*vide infra*). While the water molecules bound in the bulk crystal structure require thermal energy to be liberated as shown by previous thermogravimetric studies,[59,71] the weakly adsorbed surface water molecules or crystal water in the surface region that may be weakly bound are expected to be removed without much energy input. The first cycle also exhibits a large hysteresis, which is caused by the replenishment of the surface-bound water or crystalline water in the surface region that was lost during the drying stage. The relative mass change over each stage of HAP remains consistent, but in the case of struvite, over each successive step, the higher adsorbed mass of water decreases, as indicated by the decreasing relative mass change. This leads to a higher starting mass at the beginning of each cycle, indicating that the sample mass increases over each cycle by taking up some water that does not leave during the desorption portion of the cycle. This observation supports the hypothesis of surface water that was lost during the drying stage, which is replenished over the adsorption cycles. Such reversible water adsorption/desorption and resulting crystal structure changes have been reported previously on low-solubility materials, indicating that hydrate structures exhibit varying stabilities under relative humidity.[72] The relative mass change of struvite over the 24 h drying period at 0% RH cannot be assigned only to the surface water loss, as a low surface area material is not expected to lose significant mass purely from surface water loss. It can be proposed that the loss of crystalline water leads to changes in the hexahydrate structure, and thus, a 10 min drying time was used in subsequent experiments, with four cycles of adsorption/desorption to study the effect of shorter 0% RH steps.

Figure 6c demonstrates the relative mass change and target RH over the experiment as a function of time with no prolonged drying, as no dramatic mass loss is observed.

https://doi.org/10.1021/acsearthspacechem.1c00406
ACS Earth Space Chem. 2022, 6, 431−443

However, the first adsorption cycle shows a large uptake that is irreversible in the desorption branch of the experiment. This observation is consistent with the previous experiment with 24 h of drying, leading to the conclusion that struvite undergoes a surface hydration step that occurs regardless of the initial drying treatment. In contrast to the experiment with the 24 h drying step where the maximum relative mass change was ∼0.8%, the 10 min drying step leads to a slightly smaller initial uptake closer to 0.6%, showing that the shorter drying time may not have caused the same water loss from the crystal structure compared to the longer drying time. This large uptake of water during the first adsorption cycle leads to an unusual isotherm as shown in Figure 6d for the experiment with the 10 min drying step, which is similar to that of the experiment with a 24 h drying step. Furthermore, both experiments lead to a first cycle with a significant hysteresis loop. The hysteresis is caused by the large uptake in the adsorption branch and the relatively small desorption branch. This discrepancy between the adsorption and desorption branches indicates that the hydration occurring in the first cycle of adsorption leads to a permanent change in the struvite surface structure. The subsequent three cycles show consistent behavior with no significant variations in the isotherms (Figure 6d). Compared to the first cycle where significant surface restructuring is occurring, cycles 2−4 do not show such a drastic difference between adsorption and desorption branches. Therefore, model fits are performed using cycles 2−4 for struvite in this work to avoid the surface restructuring, which would inevitably disagree with common assumptions of Brunauer−Emmett−Teller (BET) and Freundlich equations.

Water Adsorption Isotherms on HAP and Struvite. The BET equation is the most widely used equation to calculate adsorption parameters such as monolayer coverage and surface area of adsorbent materials.[63,73] In this work, the BET equation is used to calculate the monolayer coverage of water and surface area of HAP and struvite during the adsorption branch. Equation 1 shows the BET equation used for monolayer coverage calculation

$$\frac{1}{V_a\left(\frac{P_0}{P}-1\right)} = \frac{C-1}{V_m C}\cdot\frac{P}{P_0} + \frac{1}{V_m C} \tag{1}$$

The P/P_0 variable signifies the relative pressure of the adsorbate molecule of interest, which is varied from 0 to 0.95 in this study. The range of data between 0.05 and 0.35 was used for fitting the linear BET equation since the region where monolayer adsorption occurs is preferred.[63] The parameters V_a and V_m denote the volume of adsorbed molecules and the specific monolayer capacity, respectively. The C parameter is a BET sorption constant, which is exponentially related to the monolayer adsorption energy.[63] The BET specific surface area was calculated using a molecular cross-sectional area of 0.125 nm^2 for a water molecule.[74] The BET model is based on Langmuir adsorption, which adheres to the following assumptions.[63] Namely, (1) the adsorbate−surface interaction energy is the same for all surface sites, (2) the surface adsorption site is defined as the area on the surface where the adsorbate binds to the surface, (3) adsorption of molecules on the surface occurs independent of the neighboring adsorbate molecules, (4) the activity of the adsorbate is directly proportional to the concentration in the gas phase, (5) a monolayer is formed by the adsorbate adsorption, and (6) each active site can host only one adsorbate. The BET model extends the assumptions to account for multilayer adsorption by assuming that different layers do not interact with each other.

HAP and struvite adsorption data were fitted to the BET model as shown in Figure 7 to calculate surface area and monolayer capacity. The BET fitting was done over the range of 5−35% RH as this range is used for type II isotherms, as discussed in previous literature reports.[63] Across all three cycles, HAP indicates a strong fit to the BET model (as shown in Figure 7a−c) with $R^2 > 0.9$. HAP exhibits a monolayer capacity in the range of 3.0×10^{-5} to 4.3×10^{-5} mol/g over the three cycles, while the calculated surface area (S_{BET}) varied between 1.83 and 2.74 m^2/g. Previous reports on HAP have shown higher monolayer capacity values in the range of 8.9×10^{-5} to 2.5×10^{-3} mol/g, but these HAP samples exhibited higher porosity and surface area, as well as nanostructure, which lead to higher monolayer capacities.[34,35] In contrast to HAP, struvite shows a low R^2 values (under 0.9) across all three cycles (Figure 7d−f). The surface instability evidenced by the water loss discussed earlier may be the reason for the weak fit of the adsorption data to the BET model, which does not apply to heterogeneous or dynamic surfaces. HAP does not contain significant crystal water, so it does not show this reversible water loss and thus fits the BET model with higher R^2 values. In all cases, the HAP and struvite C parameters exceed 1, which is a characteristic behavior for type II adsorption.[63] The monolayer capacity for struvite is in the range of 1.2×10^{-6} to 2.3×10^{-6} mol/g, which is consistently an order of magnitude lower than that of HAP. Similarly, the surface area for struvite is also an order of magnitude lower than that of HAP, as it was measured to be in the range of 0.07−0.14 m^2/g. The lower monolayer coverage of struvite is due to this lower surface area.

Provided the low quality of fit to the BET equation in the case of struvite, the conclusion that the struvite surface does not represent the basic assumptions of the BET model can be drawn, and thus, the Freundlich model can be applied as an alternative method of interpreting the adsorption data. The surface heterogeneity can be caused by hydrogen bonding with surface hydroxyl groups, and this can cause deviations from the BET model, which assumes uniform adsorption.[63] The Freundlich model, in contrast, does not assume uniform surface adsorption but accounts for heterogeneity.[1] The Freundlich equation is shown by eq 2. This empirical equation is used to model the adsorption of gas molecules on a heterogeneous surface with an exponential energy distribution of adsorption[75]

$$\frac{x}{m} = K_F\left(\frac{P}{P_0}\right)^{1/n} \tag{2}$$

The K_F term denotes a Freundlich equilibrium constant, while n denotes a fitting coefficient that is indicative of the binding affinity on the adsorbent surface. The K_F term is dependent on temperature. The terms x and m denote the mass change (in mg) and the total dry sample mass (in mg), while P/P_0 denotes the relative pressure of the adsorbate gas. The Freundlich equation has been applied over a wide variety of adsorption reactions, and it is applicable for both solid−liquid and solid−gas interfaces.[1,5,76,77] The Freundlich equation was applied to the two linear regions in the low RH region (0−20%) and high RH range (25−60%).

https://doi.org/10.1021/acsearthspacechem.1c00406
ACS Earth Space Chem. 2022, 6, 431−443

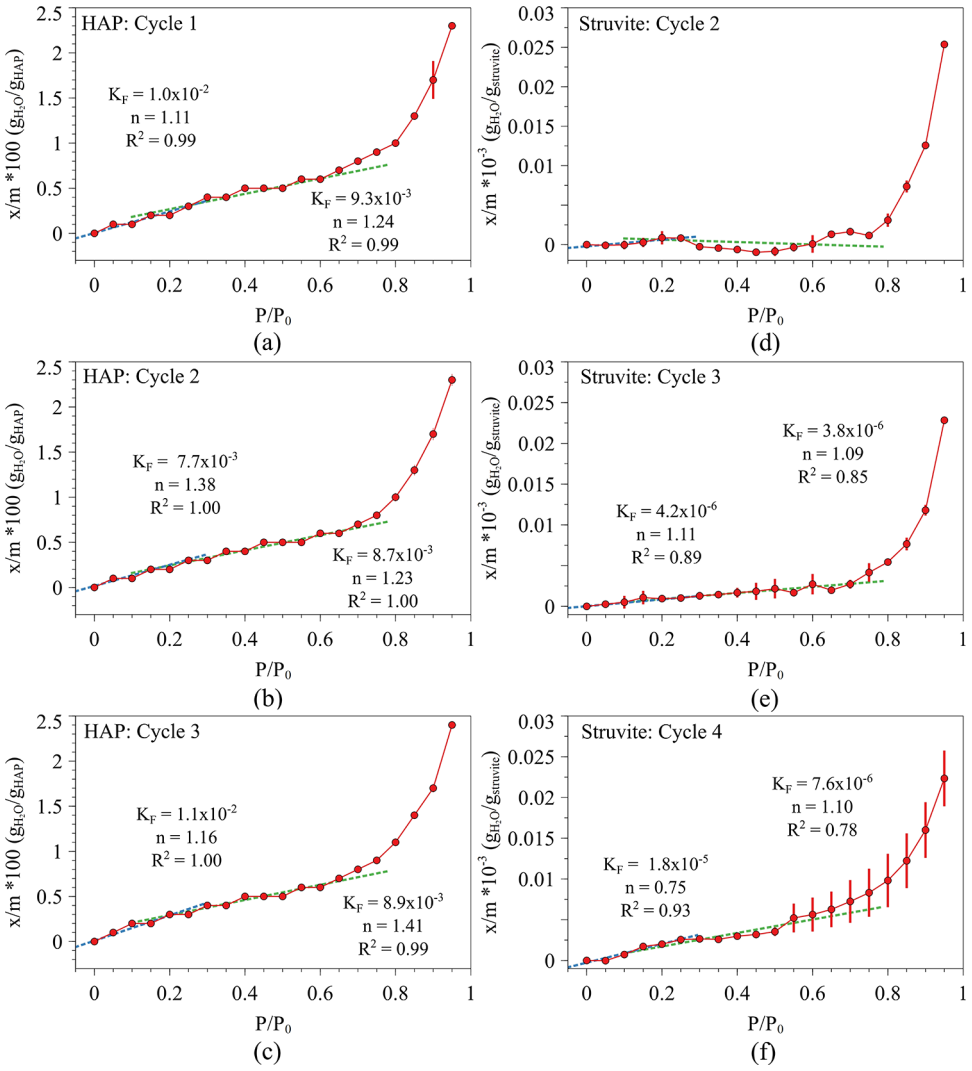

Figure 8. Freundlich adsorption isotherms for (a)−(c) HAP and (d)−(f) struvite.

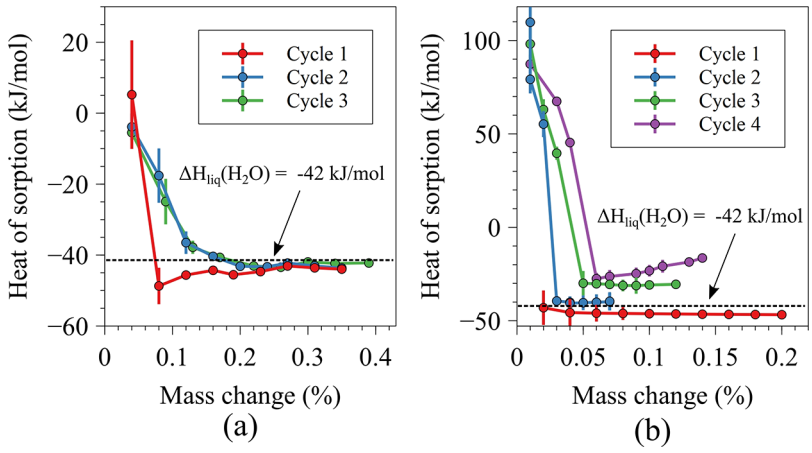

Figure 9. Heat of adsorption as a function of mass change: (a) HAP and (b) struvite.

The adsorption data and Freundlich model fits for HAP are shown in Figure 8a−c and for struvite are shown in Figure 8d−f. HAP shows good agreement with the Freundlich model in both linear regions 0−20 and 25−60% with R^2 values equal to or above 0.99. The K_F parameters for HAP in the 0−20% RH region of cycles 1, 2, and 3 were 1.0 × 10^{-2}, 7.7 × 10^{-3}, and 1.1 × 10^{-2}, respectively. The K_F parameters in the 25−60% RH range for cycles 1, 2, and 3 were 9.3 × 10^{-3}, 8.7 × 10^{-3}, and 8.9 × 10^{-3}, respectively. The n parameters for the 0−20% region in HAP in cycles 1, 2, and 3 are 1.11, 1.38, and 1.16, while in the 25−60% region are 1.24, 1.23, and 1.41. The struvite adsorption data do not fit the Freundlich equation in either

https://doi.org/10.1021/acsearthspacechem.1c00406
ACS Earth Space Chem. 2022, 6, 431−443

RH regime with acceptable R^2 values across all three cycles, with cycle 2 not showing adsorption data that could be fitted to the Freundlich model due to negative x/m values. Struvite relative mass change values during the adsorption branch of the 2nd cycle show some negative values across both of the duplicate experiments on separate struvite samples, leading to this poor fit. Cycles 3 and 4 fit the Freundlich model with R^2 values under 0.93. The K_F values for the 0−20% RH range of cycles 3 and 4 were 4.2×10^{-6} and 1.8×10^{-5}, while the values for the 25−60% range were 3.8×10^{-6} and 7.6×10^{-6}, respectively. The n values for the 0−20% RH range of cycles 3 and 4 were 1.11 and 0.75, while the values for the 25−60% range were 1.09 and 1.11, respectively. The struvite K_F values were 3−4 orders of magnitude smaller compared to HAP, while n values were largely similar. This indicates that the adsorption strength between water and the adsorbent surface is similar for the two materials, while the Freundlich adsorption capacity of water is larger for HAP.

Water as Relative Humidity Adsorption Thermodynamics. The Clausius−Clapeyron equation shown by eq 3 was used to calculate the isosteric heat of sorption

$$\ln\left(\frac{P_1}{P_2}\right) = \frac{-\Delta H_{ads}}{R}\left(\frac{1}{T_1} - \frac{1}{T_2}\right) \quad (3)$$

The heat of sorption for an adsorption process can be calculated if the two pressure values (P_1 and P_2) are known for two temperature values (T_1 and T_2). R denotes the universal gas constant and ΔH_{ads} denotes the isosteric heat of sorption. Figure 9 shows the heat of sorption calculated for HAP and struvite, using the water adsorption data as a function of the mass change. Figure 9a shows the heat of sorption for HAP. The isosteric heat of sorption becomes more negative as the amount of water adsorbed increases. The variation of the heat of sorption in the initial stage (under 0.1% mass change) is attributed to the heterogeneity of the surface and the interaction of the adsorbate water molecules with each other. As more water adsorbs on the HAP surface, the heat of sorption approaches −42 kJ/mol, which is approximately the heat of condensation for water.[78] Such behavior is consistent with the previous work on HAP[79] and has also been observed in ZnO in the previous work where a monolayer of water is formed initially, followed by multilayer adsorption, which approaches the heat of liquefication of water due to the formation of a water layer on the surface where the incoming adsorbate water interacts with the already adsorbed water instead of the surface of the material.[78] In contrast, struvite shows strikingly different behavior (Figure 9b). The values calculated from the first adsorption branch converge to the approximate heat of condensation for water (similar to HAP), but all subsequent cycles exhibit a positive heat of sorption values in the lower coverages, which become negative as more water adsorbs. The heat of sorption values for cycles 2, 3, and 4 on struvite converge to less-negative values than the heat of liquefication of water and furthermore become more positive with each cycle at the same coverage values. The surface instability evidenced by variations across all four cycles of water adsorption on struvite is most likely the cause of the large variations of the heat of sorption across all four cycles. Unlike HAP where the multilayer adsorption leads to the heat of sorption to converge to the heat of liquefication of water, struvite does not exhibit such stable adsorption behavior, leading to nonconvergent values.

DRIFTS Study of HAP and Struvite Surface Stability. The quality of the isotherm fit to adsorption data depends on the nature of the adsorbate−surface interactions, as well as the surface stability of the adsorbent. Therefore, assessing the surface stability of HAP and struvite becomes a key consideration in choosing the appropriate models to describe water adsorption data. DRIFTS studies were conducted to assess the stability of the HAP and struvite surfaces and to specifically understand the dynamic nature of the struvite surface during the drying stage, which led to anomalous adsorption behavior, as discussed in the previous section. Figure 10 shows the spectra of HAP and struvite under (<1% RH) dry airflow. As shown in Figure 10a,b, HAP does not undergo any significant changes during the drying, as also evidenced via the DVS studies as the relative mass change of HAP remained constant over time during the drying stage. The 3571 cm^{-1} band is assigned to the stretching mode of OH^- ions.[48] The broad region centered around 3400 cm^{-1} is assigned to the hydrogen-bonded OH groups present on HAP. The 1086 cm^{-1} is assigned to the ν_3 PO_4 mode, while the 962

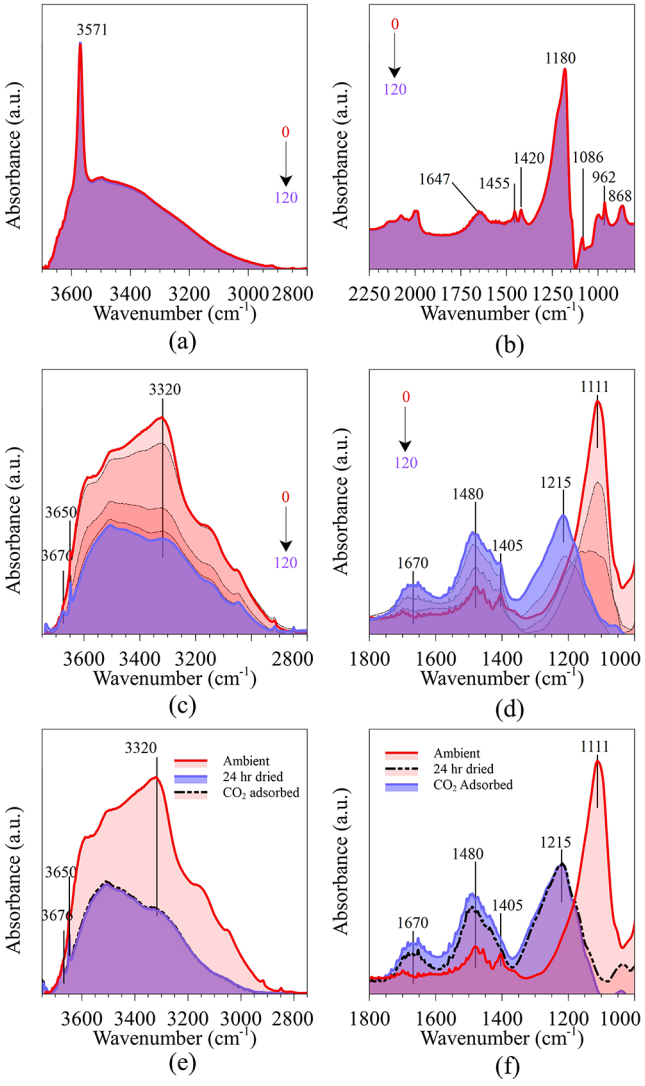

Figure 10. DRIFTS spectra under airflow at times 0, 30, 60, and 120 min for (a,b) HAP, (c,d) struvite, and (e,f) CO_2 adsorption study on struvite.

https://doi.org/10.1021/acsearthspacechem.1c00406
ACS Earth Space Chem. 2022, 6, 431−443

cm^{-1} band is assigned to the ν_1 PO_4. The 1455 and 1410 cm^{-1} bands are assigned to the ν_3 mode of a trace amount of CO_3^{2-}.[48,80] The 1647 and 1180 cm^{-1} bands are assigned to the δ(COH) bicarbonate.[60,80,81] The 868 cm^{-1} band is assigned to the HPO_4^{2-} impurities present in HAP.[48] The HAP structure remains stable throughout the drying period, indicating that the stable surface leads to adsorption data that is well described using conventional adsorption models.

Struvite DRIFTS spectra over the drying period are shown in Figure 10c,d. The struvite surface changes significantly over the drying time. Struvite exhibits a broad hydrogen-bonded water−ammonium region centered around 3320 cm^{-1}, shown in Figure 10c.[47] This region undergoes significant change over 2 h of drying, as the band intensity decreases and the shape of the band changes. As some surface water is removed, the emergence of sharper 3650 and 3676 cm^{-1} bands is observed. These sharp bands that appear after losing water may be attributed to the formation of isolated crystalline ammonium units that are no longer close to the Mg^{2+} hydration shell, bicarbonate groups,[82] as well as the recently reported dangling OH group, which does not undergo hydrogen bonding and thus is shifted to a high frequency.[50] Figure 10d shows the lower wavenumber region for the DRIFTS spectra of struvite under drying conditions. This region exhibits structural complexity due to the presence of ammonium and hydroxyl bending modes, as well as various carbonate/bicarbonate modes. Stefov et al. have conducted extensive work on struvite Fourier transform infrared spectroscopy (FTIR) as well as its multiple isomorphous analogues (wherein NH_4^+ units are replaced by other cations).[45,47] A study using deuterated ammonium ions showed that 1480 cm^{-1} can be assigned to the ν_4 mode of NH_4^+.[45] Due to significant overlap in the 1800−1300 region, assigning between carbonate modes and ammonium modes becomes nontrivial. Computational work of struvite reports that 1670 cm^{-1} can be either H−N−H or H−O−H bending modes,[50] whereas HAP (which lacks NH_4 units) contains bicarbonate bands in this region.[48]

Finally, CO_2 adsorption was used to determine whether 1670, 1405, and 1215 cm^{-1} bands are carbonate/bicarbonate species. Figure 10e shows the high wavenumber region for the CO_2 adsorption experiment, and no appreciable changes were observed in this region. Figure 10f shows the low wavenumber region, and there is no change in the 1215 cm^{-1} band, while 1670 and 1405 cm^{-1} bands show minor changes. Therefore, bicarbonates and carbonates are not expected to be a major fraction of the surface species, and as such, the low wavenumber bands are expected to be consistent with the hydroxyl and ammonium bending modes, as shown with previous computational and experimental work.[45,50] The 1405 cm^{-1} species is assigned to the ν_2 mode of NH_4^+, while the 1650 cm^{-1} band may be assigned to both water and ammonium bending modes.[50] DRIFTS studies definitively show that struvite undergoes some degree of dehydration under dry airflow and that leads to reconstruction phenomena occurring on the surface. This surface instability can be seen as one reason for the deviation from the typical heat of sorption trends (observed in HAP) on struvite as the adsorption does not follow the ideal behavior of monolayer formation, and subsequent multilayer formation, due to the transient nature of the surface water structure.

CONCLUSIONS AND ENVIRONMENTAL IMPLICATIONS

The environmental and health effects of N and P fertilizers, long an established area of research importance, are of late gaining a great deal of public interest. For example, beyond several scientific studies recently published on the topic, commentaries have appeared over the past few years in both the scientific literature and more broadly disseminated periodicals and popular media such as newspapers (see Nitrogen Triggers Extra-Toxic Algal Blooms in Lake Erie and the related scientific discussion in refs 83, 84). It is now evident that mineral fertilizers in general, due to their extensive use, result in negative effects on the environment, including groundwater contamination, eutrophication of freshwater and estuarine ecosystems, tropospheric pollution related to emissions of nitrogen oxides and ammonia gas, and accumulation of nitrous oxide (N_2O), a potent greenhouse gas that depletes the stratospheric ozone.[65,85−91] To decrease the corresponding reactive N and P nutrient influx, their recovery from various wastewater streams is gaining importance and is projected to significantly increase to provide a path toward more sustainable development. As the influx of the recovered fertilizer materials expands and the associated delivery to soil becomes even more widespread, there are many outstanding questions, and thus opportunities for research, related to the consequences that they may have on the environment.

In this work, struvite and HAP have been identified as important anthropogenically derived sources of nutrients returned to the environment at an increasing rate. However, their hygroscopic properties that will affect their dissolution rates and heterogeneous reactivity are poorly understood. HAP was shown to have a stable surface that provides water adsorption data modeled by both the BET and Freundlich models. HAP has been recently reported as a matrix for novel controlled-release urea-based nitrogen fertilizer materials due to its insoluble nature.[28,30,92] The findings in this study regarding its stability under high RH conditions show that such fertilizer applications would find success under a variety of RH conditions. In contrast to HAP, struvite exhibits a complex behavior of surface instability. The surface-bound water, as well as some fraction of the crystal water, indicates the propensity to be removed under dry airflow as shown by DVS and DRIFTS experiments, leading to significant structural alteration of the surface region. This loss of water causes complex water adsorption isotherms for struvite, which are not accurately modeled by BET or Freundlich models, which do not account for complex surface restructuring phenomena. These novel findings of the unstable struvite surface have implications for its use as a fertilizer material under varying RH conditions due to the proclivity to undergo surface restructuring.

AUTHOR INFORMATION

Corresponding Author

Jonas Baltrusaitis − *Department of Chemical and Biomolecular Engineering, Lehigh University, Bethlehem, Pennsylvania 18015, United States;* orcid.org/0000-0001-5634-955X; Phone: +1-610-758-6836; Email: job314@lehigh.edu

https://doi.org/10.1021/acsearthspacechem.1c00406
ACS Earth Space Chem. 2022, 6, 431−443

Authors

Manoj Silva − *Department of Chemical and Biomolecular Engineering, Lehigh University, Bethlehem, Pennsylvania 18015, United States;* orcid.org/0000-0002-5353-006X

John P. Baltrus − *National Energy Technology Laboratory, U.S. Department of Energy, Pittsburgh, Pennsylvania 15236, United States*

Daniel J. Burnett − *Surface Measurements Systems North America, Allentown, Pennsylvania 18103, United States*

Complete contact information is available at: https://pubs.acs.org/10.1021/acsearthspacechem.1c00406

Notes

The authors declare no competing financial interest.

■ ACKNOWLEDGMENTS

This material was based upon work supported by the National Science Foundation under Grant No. CHE 1710120.

■ REFERENCES

(1) Hatch, C. D.; Wiese, J. S.; Crane, C. C.; Harris, K. J.; Kloss, H. G.; Baltrusaitis, J. Water adsorption on clay minerals as a function of relative humidity: Application of BET and Freundlich adsorption models. *Langmuir* **2012**, *28*, 1790−1803.

(2) Rubasinghege, G.; Grassian, V. H. Role(s) of adsorbed water in the surface chemistry of environmental interfaces. *Chem. Commun.* **2013**, *49*, 3071−3094.

(3) Al-Hosney, H. A.; Grassian, V. H. Water, sulfur dioxide and nitric acid adsorption on calcium carbonate: A transmission and ATR-FTIR study. *Phys. Chem. Chem. Phys.* **2005**, *7*, 1266−1276.

(4) Rahaman, A.; Grassian, V. H.; Margulis, C. J. Dynamics of water adsorption onto a calcite surface as a function of relative humidity. *J. Phys. Chem. C* **2008**, *112*, 2109−2115.

(5) Peng, C.; Gu, W.; Li, R.; Lin, Q.; Ma, Q.; Jia, S.; Krishnan, P.; Wang, X.; Tang, M. Large Variations in Hygroscopic Properties of Unconventional Mineral Dust. *ACS Earth Space Chem.* **2020**, *4*, 1823−1830.

(6) Kim, D.; Xiao, Y.; Karchere-Sun, R.; Richmond, E.; Ricker, H. M.; Leonardi, A.; Navea, J. G. Atmospheric Processing of Anthropogenic Combustion Particles: Effects of Acid Media and Solar Flux on the Iron Mobility from Fly Ash. *ACS Earth Space Chem.* **2020**, *4*, 750−761.

(7) Navea, J. G.; Richmond, E.; Stortini, T.; Greenspan, J. Water Adsorption Isotherms on Fly Ash from Several Sources. *Langmuir* **2017**, *33*, 10161−10171.

(8) Tang, M.; Cziczo, D. J.; Grassian, V. H. Interactions of Water with Mineral Dust Aerosol: Water Adsorption, Hygroscopicity, Cloud Condensation, and Ice Nucleation. *Chemical Reviews* **2016**, *116*, 4205−4259.

(9) Scanza, R. A.; Mahowald, N.; Ghan, S.; Zender, C. S.; Kok, J. F.; Liu, X.; Zhang, Y.; Albani, S. Modeling dust as component minerals in the Community Atmosphere Model: Development of framework and impact on radiative forcing. *Atmos. Chem. Phys.* **2015**, *15*, 537−561.

(10) Paytan, A.; McLaughlin, K. The oceanic phosphorus cycle. *Chem. Rev.* **2007**, *107*, 563−576.

(11) Stockdale, A.; Krom, M. D.; Mortimer, R. J. G.; Benning, L. G.; Carslaw, K. S.; Herbert, R. J.; Shi, Z.; Myriokefalitakis, S.; Kanakidou, M.; Nenes, A. Understanding the nature of atmospheric acid processing of mineral dusts in supplying bioavailable phosphorus to the oceans. *Proc. Natl. Acad. Sci. U.S.A.* **2016**, *113*, 14639−14644.

(12) Yu, H.; Chin, M.; Yuan, T.; Bian, H.; Remer, L. A.; Prospero, J. M.; Omar, A.; Winker, D.; Yang, Y.; Zhang, Y.; et al. The fertilizing role of African dust in the Amazon rainforest: A first multiyear assessment based on data from Cloud-Aerosol Lidar and Infrared Pathfinder Satellite Observations. *Geophys. Res. Lett.* **2015**, *42*, 1984−1991.

(13) Migon, C.; Sandroni, V.; Béthoux, J. P. Atmospheric input of anthropogenic phosphorus to the northwest Mediterranean under oligotrophic conditions. *Mar. Environ. Res.* **2001**, *52*, 413−426.

(14) Mayer, B. K.; Baker, L. A.; Boyer, T. H.; Drechsel, P.; Gifford, M.; Hanjra, M. A.; Parameswaran, P.; Stoltzfus, J.; Westerhoff, P.; Rittmann, B. E. Total Value of Phosphorus Recovery. *Environ. Sci. Technol.* **2016**, *50*, 6606−6620.

(15) Rittmann, B. E.; Mayer, B.; Westerhoff, P.; Edwards, M. Capturing the lost phosphorus. *Chemosphere* **2011**, *84*, 846−853.

(16) Bouwman, L.; Goldewijk, K. K.; Van Der Hoek, K. W.; Beusen, A. H. W.; Van Vuuren, D. P.; Willems, J.; Rufino, M. C.; Stehfest, E. Exploring global changes in nitrogen and phosphorus cycles in agriculture induced by livestock production over the 1900−2050 period. *Proc. Natl. Acad. Sci. U.S.A.* **2013**, *110*, 20882−20887.

(17) Morée, A. L.; Beusen, A. H. W.; Bouwman, A. F.; Willems, W. J. Exploring global nitrogen and phosphorus flows in urban wastes during the twentieth century. *Global Biogeochem. Cycles* **2013**, *27*, 836−846.

(18) Dodds, W. K.; Bouska, W. W.; Eitzmann, J. L.; Pilger, T. J.; Pitts, K. L.; Riley, A. J.; Schloesser, J. T.; Thornbrugh, D. J. Eutrophication of U. S. freshwaters: Analysis of potential economic damages. *Environ. Sci. Technol.* **2009**, *43*, 12−19.

(19) Dodds, W. K.; Smith, V. H. Nitrogen, phosphorus, and eutrophication in streams. *Inland Waters* **2016**, *6*, 155−164.

(20) Yamagata, Y.; Watanabe, H.; Saitoh, M.; Namba, T. Volcanic production of polyphosphates and its relevance to prebiotic evolution. *Nature* **1991**, *352*, 516−519.

(21) Ridame, C.; Guieu, C. Saharan input of phosphate to the oligotrophic water of the open western Mediterranean Sea. *Limnol. Oceanogr.* **2002**, *47*, 856−869.

(22) Kiani, D.; Sheng, Y.; Lu, B.; Barauskas, D.; Honer, K.; Jiang, Z.; Baltrusaitis, J. Transient Struvite Formation during Stoichiometric (1:1) NH4+ and PO43− Adsorption/Reaction on Magnesium Oxide (MgO) Particles. *ACS Sustainable Chem. Eng.* **2018**, *7*, 1545−1556.

(23) Silva, M.; Murzin, V.; Zhang, L.; Baltrus, J. P.; Baltrusaitis, J. Transition metal doped MgO nanoparticles for nutrient recycling: An alternate Mg source for struvite synthesis from wastewater. *Environ. Sci.: Nano* **2020**, *7*, 3482−3496.

(24) Silva, M.; Baltrusaitis, J. A review of phosphate adsorption on Mg-containing materials: kinetics, equilibrium, and mechanistic insights. *Environ. Sci. Water Res. Technol.* **2020**, *12*, 3178−3194.

(25) Lu, B.; Kiani, D.; Taifan, W.; Barauskas, D.; Honer, K.; Zhang, L.; Baltrusaitis, J. Spatially Resolved Product Speciation during Struvite Synthesis from Magnesite (MgCO3) Particles in Ammonium (NH 4 +) and Phosphate (PO_4^{3-}) Aqueous Solutions. *J. Phys. Chem. C* **2019**, *123*, 8908−8922.

(26) Kiani, D.; Silva, M.; Sheng, Y.; Baltrusaitis, J. Experimental Insights into the Genesis and Growth of Struvite Particles on Low-Solubility Dolomite Mineral Surfaces. *J. Phys. Chem. C* **2019**, *123*, 25135−25145.

(27) Chen, L.; Zhou, C. H.; Zhang, H.; Tong, D. S.; Yu, W. H.; Yang, H. M.; Chu, M. Q. Capture and recycling of ammonium by dolomite-aided struvite precipitation and thermolysis. *Chemosphere* **2017**, *187*, 302−310.

(28) Rop, K.; Karuku, G. N.; Mbui, D.; Michira, I.; Njomo, N. Formulation of slow release NPK fertilizer (cellulose-graft-poly-(acrylamide)/nano-hydroxyapatite/soluble fertilizer) composite and evaluating its N mineralization potential. *Ann. Agric. Sci.* **2018**, *63*, 163−172.

(29) Jones, D. L.; Roose, T.; Talboys, P. J.; Healey, J. R.; Withers, P. J. A. Struvite: a slow-release fertiliser for sustainable phosphorus management? *Plant Soil* **2016**, *401*, 109−123.

(30) Kottegoda, N.; Munaweera, I.; Adassooriya, N.; Karunaratne, V. A green slow-release fertilizer composition based on urea-modified hydroxyapatite nanoparticles encapsulated wood. *Curr. Sci.* **2011**, *101*, 73−78.

(31) Cid, C. A.; Jasper, J. T.; Hoffmann, M. R. Phosphate Recovery from Human Waste via the Formation of Hydroxyapatite during

Electrochemical Wastewater Treatment. *ACS Sustainable Chem. Eng.* **2018**, *6*, 3135−3142.
(32) Rahaman, M. S.; Mavinic, D. S.; Bhuiyan, M. I. H.; Koch, F. A. Exploring the determination of struvite solubility product from analytical results. *Environ. Technol.* **2006**, *27*, 951−961.
(33) Bell, L. C.; Mika, H.; Kruger, B. J. Synthetic hydroxyapatite-solubility product and stoichiometry of dissolution. *Arch. Oral Biol.* **1978**, *23*, 329−336.
(34) Miyauchi, M.; Watanabe, T.; Hoshi, D.; Ohba, T. Irreversible adsorption of acidic, basic, and water gas molecules on calcium-deficient hydroxyapatite. *Dalton Trans.* **2019**, *48*, 17507−17515.
(35) Szałaj, U.; Świderska-Środa, A.; Chodara, A.; Gierlotka, S.; Łojkowski, W. Nanoparticle Size Effect on Water Vapour Adsorption by Hydroxyapatite. *Nanomaterials* **2019**, *9*, No. 1005.
(36) Shen, W.; Li, X.; Lu, X.; Guo, W.; Zhou, S.; Wan, Y. Experimental study and isotherm models of water vapor adsorption in shale rocks. *J. Nat. Gas Sci. Eng.* **2018**, *52*, 484−491.
(37) Limousin, G.; Gaudet, J. P.; Charlet, L.; Szenknect, S.; Barthès, V.; Krimissa, M. Sorption isotherms: A review on physical bases, modeling and measurement. *Appl. Geochem.* **2007**, *22*, 249−275.
(38) Fairley, N.; Fernandez, V.; Richard-Plouet, M.; Guillot-Deudon, C.; Walton, J.; Smith, E.; Flahaut, D.; Greiner, M.; Biesinger, M.; Tougaard, S.; et al. Systematic and collaborative approach to problem solving using X-ray photoelectron spectroscopy. *Appl. Surf. Sci. Adv.* **2021**, *5*, No. 100112.
(39) Fara, A. N. K. A.; Abdullah, H. Z. In *Characterization of Derived Natural Hydroxyapatite (HAp) Obtained from Different Types of Tilapia Fish Bones and Scales*, AIP Conference Proceedings; American Institute of Physics Inc., 2015; p 020077.
(40) Rincón-López, J. A.; Hermann-Muñoz, J. A.; Giraldo-Betancur, A. L.; Vizcaya-Ruiz, D.; Alvarado-Orozco, J. M.; Muñoz-Saldaña, J. Synthesis, Characterization and In Vitro Study of Synthetic and Bovine-Derived Hydroxyapatite Ceramics: A Comparison. *Materials* **2018**, *11*, No. 333.
(41) Ben Osman, M.; Krafft, J. M.; Millot, Y.; Averseng, F.; Yoshioka, T.; Kubo, J.; Costentin, G. Molecular Understanding of the Bulk Composition of Crystalline Nonstoichiometric Hydroxyapatites: Application to the Rationalization of Structure−Reactivity Relationships. *Eur. J. Inorg. Chem.* **2016**, *2016*, 2709−2720.
(42) Shaddel, S.; Ucar, S.; Andreassen, J. P.; Sterhus, S. W. Engineering of struvite crystals by regulating supersaturation—Correlation with phosphorus recovery, crystal morphology and process efficiency. *J. Environ. Chem. Eng.* **2019**, *7*, No. 102918.
(43) Takagi, S.; Mathew, M.; Brown, W. E. Crystal structures of bobierrite and synthetic Mg3(PO4)2·8H2O. *Am. Mineral.* **1986**, *71*, 1229−1233.
(44) Kongshaug, K. O.; Fjellvåg, H.; Lillerud, K. P. The synthesis and crystal structure of a hydrated magnesium phosphate Mg3-(PO4)2·4H2O. *Solid State Sci.* **2001**, *3*, 353−359.
(45) Stefov, V.; Šoptrajanov, B.; Spirovski, F.; Kuzmanovski, I.; Lutz, H.; Engelen, B. Infrared and Raman spectra of magnesium ammonium phosphate hexahydrate (struvite) and its isomorphous analogues. I. Spectra of protiated and partially deuterated magnesium potassium phosphate hexahydrate. *J. Mol. Struct.* **2004**, *689*, 1−10.
(46) Stefov, V.; Cahil, A.; Šoptrajanov, B.; Najdoski, M.; Spirovski, F.; Engelen, B.; Lutz, H. D.; Koleva, V. Infrared and Raman spectra of magnesium ammonium phosphate hexahydrate (struvite) and its isomorphous analogues. VII: Spectra of protiated and partially deuterated hexagonal magnesium caesium phosphate hexahydrate. *J. Mol. Struct.* **2009**, *924*−*926*, 100−106.
(47) Stefov, V.; Šoptrajanov, B.; Kuzmanovski, I.; Lutz, H. D.; Engelen, B. Infrared and Raman spectra of magnesium ammonium phosphate hexahydrate (struvite) and its isomorphous analogues. III. Spectra of protiated and partially deuterated magnesium ammonium phosphate hexahydrate. *J. Mol. Struct.* **2005**, *752*, 60−67.
(48) Markovic, M.; Fowler, B. O.; Tung, M. S. Preparation and Comprehensive Characterization of a Calcium Hydroxyapatite Reference Material. *J. Res. Natl. Inst. Stand. Technol.* **2004**, *109*, No. 553.
(49) Frost, R. L.; Weier, M. L.; Martens, W. N.; Henry, D. A.; Mills, S. J. Raman spectroscopy of newberyite, hannayite and struvite. *Spectrochim. Acta, Part A* **2005**, *62*, 181−188.
(50) Sidorczuk, D.; Kozanecki, M.; Civalleri, B.; Pernal, K.; Prywer, J. Structural and Optical Properties of Struvite. Elucidating Structure of Infrared Spectrum in High Frequency Range. *J. Phys. Chem. A* **2020**, *124*, 8668−8678.
(51) Hövelmann, J.; Stawski, T. M.; Freeman, H. M.; Besselink, R.; Mayanna, S.; Perez, J. P. H.; Hondow, N. S.; Benning, L. G. Struvite Crystallisation and the Effect of Co2+ Ions. *Minerals* **2019**, *9*, No. 503.
(52) Wang, F.; Fu, R.; Lv, H.; Zhu, G.; Lu, B.; Zhou, Z.; Wu, X.; Chen, H. Phosphate Recovery from Swine Wastewater by a Struvite Precipitation Electrolyzer. *Sci. Rep.* **2019**, *9*, No. 8893.
(53) Hövelmann, J.; Stawski, T. M.; Besselink, R.; Freeman, H. M.; Dietmann, K. M.; Mayanna, S.; Pauw, B. R.; Benning, L. G. A template-free and low temperature method for the synthesis of mesoporous magnesium phosphate with uniform pore structure and high surface area. *Nanoscale* **2019**, *11*, 6939−6951.
(54) Lu, H. B.; Campbell, C. T.; Graham, D. J.; Ratner, B. D. Surface Characterization of Hydroxyapatite and Related Calcium Phosphates by XPS and TOF-SIMS. *Anal. Chem.* **2000**, *72*, 2886−2894.
(55) Sun, B.; Zhao, H.; Zhao, Y.; Tucker, M. E.; Han, Z.; Yan, H. Bio-Precipitation of Carbonate and Phosphate Minerals Induced by the Bacterium Citrobacter freundii ZW123 in an Anaerobic Environment. *Minerals* **2020**, *10*, No. 65.
(56) Negrila, C. C.; Predoi, M. V.; Iconaru, S. L.; Predoi, D. Development of Zinc-Doped Hydroxyapatite by Sol-Gel Method for Medical Applications. *Molecules* **2018**, *23*, No. 2986.
(57) Wei, L.; Hong, T.; Hu, Z.; Luo, L.; Zhang, Q.; Chen, T. Modeling surface acid-base properties of struvite crystals synthesized in aqueous solution. *Colloids Surf., A* **2018**, *553*, 237−243.
(58) Uskoković, V. X-ray photoelectron and ion scattering spectroscopic surface analyses of amorphous and crystalline calcium phosphate nanoparticles with different chemical histories. *Phys. Chem. Chem. Phys.* **2020**, *22*, 5531−5547.
(59) Frost, R. L.; Weier, M. L.; Erickson, K. L. Thermal decomposition of struvite: Implications for the decomposition of kidney stones. *J. Therm. Anal. Calorim.* **2004**, *76*, 1025−1033.
(60) Kiani, D.; Baltrusaitis, J. Surface chemistry of hydroxyapatite for sustainable n-butanol production from bio-ethanol. *Chem. Catal.* **2021**, *1*, 782−801.
(61) Panda, R. N.; Hsieh, M. F.; Chung, R. J.; Chin, T. S. FTIR, XRD, SEM and solid state NMR investigations of carbonate-containing hydroxyapatite nano-particles synthesized by hydroxide-gel technique. *J. Phys. Chem. Solids* **2003**, *64*, 193−199.
(62) Kang, D.-H.; Jeon, S.; Yoo, H.; Ishikawa, T.; Okada, J. T.; Paradis, P.-F.; Lee, G. W. Nanosized Nucleus-Supercooled Liquid Interfacial Free Energy and Thermophysical Properties of Early and Late Transition Liquid Metals. *Cryst. Growth Des.* **2014**, *14*, 1103−1109.
(63) Thommes, M.; Kaneko, K.; Neimark, A. V.; Olivier, J. P.; Rodriguez-Reinoso, F.; Rouquerol, J.; Sing, K. S. W. Physisorption of gases, with special reference to the evaluation of surface area and pore size distribution (IUPAC Technical Report). *Pure Appl. Chem.* **2015**, *87*, 1051−1069.
(64) Sing, K. S. W.; Williams, R. T. Physisorption Hysteresis Loops and the Characterization of Nanoporous Materials. *Adsorpt. Sci. Technol.* **2016**, *22*, 773−782.
(65) Silva, M.; Barcauskaite, K.; Drapanauskaite, D.; Tian, H.; Bučko, T.; Baltrusaitis, J. Relative Humidity Facilitated Urea Particle Reaction with Salicylic Acid: A Combined In Situ Spectroscopy and DFT Study. *ACS Earth Space Chem.* **2020**, *4*, 1018−1028.
(66) Wise, M. E.; Martin, S. T.; Russell, L. M.; Buseck, P. R. Water Uptake by NaCl Particles Prior to Deliquescence and the Phase Rule. *Aerosol Sci. Technol.* **2008**, *42*, 281−294.
(67) Mazzei, L.; Broll, V.; Casali, L.; Silva, M.; Braga, D.; Grepioni, F.; Baltrusaitis, J.; Ciurli, S. Multifunctional Urea Cocrystal with Combined Ureolysis and Nitrification Inhibiting Capabilities for

Enhanced Nitrogen Management. *ACS Sustainable Chem. Eng.* **2019**, *7*, 13369−13378.
(68) Ishikawa, T.; Wakamura, M.; Kondo, S. Surface Characterization of Calcium Hydroxylapatite by Fourier Transform Infrared Spectroscopy. *Langmuir* **1989**, *5*, 140−144.
(69) Wade, J. B.; Martin, G. P.; Long, D. F. A methodological approach for determining the effect of moisture content on the compaction properties of powders: Granular hydroxyapatite. *Powder Technol.* **2013**, *246*, 511−519.
(70) LeGeros, R. Z.; Bonel, G.; Legros, R. Types of "H2O" in human enamel and in precipitated apatites. *Calcif. Tissue Res.* **1978**, *26*, 111−118.
(71) Ramlogan, M. V.; Rouff, A. A. An investigation of the thermal behavior of magnesium ammonium phosphate hexahydrate. *J. Therm. Anal. Calorim.* **2016**, *123*, 145−152.
(72) Lee, J.; Kim, D.; Park, J.; Kim, E. E.; Lah, M. S.; Kim, A. Pseudopolymorphs of LB30870, a Direct Thrombin Inhibitor: One-Dimensional Solvent Channel Structures Explain Reversible Hydration/Dehydration. *Cryst. Growth Des.* **2018**, *18*, 95−104.
(73) Brunauer, S.; Emmett, P. H.; Teller, E. Adsorption of Gases in Multimolecular Layers. *J. Am. Chem. Soc.* **1938**, *60*, 309−319.
(74) McClellan, A. L.; Harnsberger, H. F. Cross-sectional areas of molecules adsorbed on solid surfaces. *J. Colloid Interface Sci.* **1967**, *23*, 577−599.
(75) Freundlich, H. Of the adsorption of gases. Section II. Kinetics and energetics of gas adsorption. Introductory paper to section II. *Trans. Faraday Soc.* **1932**, *28*, 195−201.
(76) Ahmed, S.; Guo, Y.; Huang, R.; Li, D.; Tang, P.; Feng, Y. Hexamethylene tetramine-assisted hydrothermal synthesis of porous magnesium oxide for high-efficiency removal of phosphate in aqueous solution. *J. Environ. Chem. Eng.* **2017**, *5*, 4649−4655.
(77) Freundlich, H.; Heller, W. The Adsorption of cis- and trans-Azobenzene. *J. Am. Chem. Soc.* **1939**, *61*, 2228−2230.
(78) Nagao, M. On physisorption of water on zinc oxide surface. *J. Phys. Chem. A* **1971**, *75*, 3822−3828.
(79) Rootare, H. M.; Craig, R. G. Vapor Phase Adsorption of Water on Hydroxyapatite. *J. Dent. Res.* **1977**, *56*, 1437−1448.
(80) Diallo-Garcia, S.; Ben Osman, M.; Krafft, J.-M.; Casale, S.; Thomas, C.; Kubo, J.; Costentin, G. Identification of Surface Basic Sites and Acid−Base Pairs of Hydroxyapatite. *J. Phys. Chem. C* **2014**, *118*, 12744−12757.
(81) Hill, I. M.; Hanspal, S.; Young, Z. D.; Davis, R. J. DRIFTS of Probe Molecules Adsorbed on Magnesia, Zirconia, and Hydroxyapatite Catalysts. *J. Phys. Chem. C* **2015**, *119*, 9186−9197.
(82) Busca, G.; Lorenzelli, V. Infrared spectroscopic identification of species arising from reactive adsorption of carbon oxides on metal oxide surfaces. *Mater. Chem.* **1982**, *7*, 89−126.
(83) Paerl, H. W.; Xu, H.; Hall, N. S.; Zhu, G.; Qin, B.; Wu, Y.; Rossignol, K. L.; Dong, L.; McCarthy, M. J.; Joyner, A. R. Controlling Cyanobacterial Blooms in Hypertrophic Lake Taihu, China: Will Nitrogen Reductions Cause Replacement of Non-N2 Fixing by N2 Fixing Taxa? *PLoS One* **2014**, *9*, No. e113123.
(84) Harke, M. J.; Davis, T. W.; Watson, S. B.; Gobler, C. J. Nutrient-Controlled Niche Differentiation of Western Lake Erie Cyanobacterial Populations Revealed via Metatranscriptomic Surveys. *Environ. Sci. Technol.* **2016**, *50*, 604−615.
(85) Stocker, T. *Climate Change 2013: The Physical Science Basis: Working Group I Contribution to the Fifth Assessment Report of the Intergovernmental Panel on Climate Change*; Cambridge University Press, 2014.
(86) Zhang, X.; Davidson, E. A.; Mauzerall, D. L.; Searchinger, T. D.; Dumas, P.; Shen, Y. Managing nitrogen for sustainable development. *Nature* **2015**, *528*, 51−59.
(87) Conley, D. J.; Paerl, H. W.; Howarth, R. W.; Boesch, D. F.; Seitzinger, S. P.; Havens, K. E.; Lancelot, C.; Likens, G. E. Controlling eutrophication: Nitrogen and phosphorus. *Science* **2009**, *323*, No. 10141015.
(88) Oikawa, P. Y.; Ge, C.; Wang, J.; Eberwein, J. R.; Liang, L. L.; Allsman, L. A.; Grantz, D. A.; Jenerette, G. D. Unusually high soil nitrogen oxide emissions influence air quality in a high-temperature agricultural region. *Nat. Commun.* **2015**, *6*, No. 8753.
(89) Hewitt, C. N.; MacKenzie, A. R.; Di Carlo, P.; Di Marco, C. F.; Dorsey, J. R.; Evans, M.; Fowler, D.; Gallagher, M. W.; Hopkins, J. R.; Jones, C. E.; et al. Nitrogen management is essential to prevent tropical oil palm plantations from causing ground-level ozone pollution. *Proc. Natl. Acad. Sci. U.S.A.* **2009**, *106*, 18447−18451.
(90) Diaz, R. J.; Rosenberg, R. Spreading Dead Zones and Consequences for Marine Ecosystems. *Science* **2008**, *321*, 926−929.
(91) Duce, R. A.; LaRoche, J.; Altieri, K.; Arrigo, K. R.; Baker, A. R.; Capone, D. G.; Cornell, S.; Dentener, F.; Galloway, J.; Ganeshram, R. S.; et al. Impacts of atmospheric anthropogenic nitrogen on the open ocean. *Science* **2008**, *320*, 893−897.
(92) Abeywardana, L.; Silva, M.; Sandaruwan, C.; Dahanayake, D.; Priyadarshana, G.; Chathurika, J. A.; Kottegoda, N. Zinc-Doped Hydroxyapatite−Urea Nanoseed Coating as an Efficient Macro−Micro Plant Nutrient Delivery Agent. *ACS Agric. Sci. Technol.* **2021**, *1*, 230−239.

Recommended by ACS

Selective Interactions of Soil Organic Matter Compounds with Calcite and the Role of Aqueous Ca
Odeta Qafoku, Mark E. Bowden, *et al.*
JUNE 19, 2022
ACS EARTH AND SPACE CHEMISTRY
READ

Crystal Growth of Smectite: A Study Based on the Change in Crystal Chemistry and Morphology of Saponites with Synthesis Time
Chaoqun Zhang, Jianxi Zhu, *et al.*
NOVEMBER 27, 2019
ACS EARTH AND SPACE CHEMISTRY
READ

Competitive Adsorption Processes at Clay Mineral Surfaces: A Coupled Experimental and Modeling Approach
Esra Orucoglu, Christophe Tournassat, *et al.*
JANUARY 05, 2022
ACS EARTH AND SPACE CHEMISTRY
READ

Experimental Insights into the Genesis and Growth of Struvite Particles on Low-Solubility Dolomite Mineral Surfaces
Daniyal Kiani, Jonas Baltrusaitis, *et al.*
SEPTEMBER 24, 2019
THE JOURNAL OF PHYSICAL CHEMISTRY C
READ

Get More Suggestions >